scientific reports

OPEN

Amyloids in bladder cancer hijack cancer-related proteins and are positive correlated to tumor stage

Diego Alem[1,11 ✉], César X. García-Laviña[2], Francisco Garagorry[3], Dardo Centurión[3], Joaquina Farias[4], Hany Pazos-Espinosa[1], María Noel Cuitiño-Mendiberry[5], Carolina Villadóniga[6], Susana Castro-Sowinski[1,2,6], Martín Fló[7,8], Federico Carrión[7,9], Brenda Iglesias[10], Kevin Madauss[10] & Lucía Canclini[1,11 ✉]

Despite the current diagnostic and therapeutic approaches to bladder cancer being widely accepted, there have been few significant advancements in this field over the past decades. This underscores the necessity for a paradigm shift in the approach to bladder cancer. The role of amyloids in cancer remains unclear despite their identification in several other pathologies. In this study, we present evidence of amyloids in bladder cancer, both in vitro and in vivo. In a murine model of bladder cancer, a positive correlation was observed between amyloids and tumor stage, indicating an association between amyloids and bladder cancer progression. Subsequently, the amyloid proteome of the RT4 non-invasive and HT1197 invasive bladder cancer cell lines was identified and included oncogenes, tumor suppressors, and highly expressed cancer-related proteins. It is proposed that amyloids function as structures that sequester key proteins. Therefore, amyloids should be considered in the study and diagnosis of bladder cancer.

An amyloid is a three-dimensional structure that proteins can adopt in a different way from their native structure by folding into a very compact cross-beta motif[1]. The fundamental structure is a beta-strand segment comprising a few residues that can fold in a repetitive manner. Given that virtually all proteins contain regions capable of adopting this conformation, they are all potentially susceptible to amyloid formation[2].

The biophysical principles that underpin amyloid folding give rise to structures that exhibit a high degree of molecular order, stability, tensile strength, protease resistance, and the capacity to replicate their conformation through self-assembly templates and seeding[3].

The universality and structural properties of amyloids make them useful for functional roles[4], particularly in processes where structural stability or long-term storage is required. Examples include the bacterial proteins that serve as scaffolds for biofilm formation, a survival strategy bacteria use for antibiotics and other environmental stress resistance[5]. Additionally, secretory granule amyloids serve as a long-term storage mechanism for hormones[6], while prion-mediated memory mechanisms have been proposed in *Drosophila* and *Aplysia*[7].

Amyloids have been linked to over 50 distinct human pathologies. These include a range of neuropathological disorders, such as Alzheimer's, Parkinson's, Huntington's diseases and, amyotrophic lateral sclerosis, as well as metabolic disorders such as type 2 diabetes, and amyloidosis, a systemic condition characterized by the presence of proteinaceous deposits in various organs[8].

In cancer, amyloid folding has been proposed to be responsible for the loss and gain of function of the p53 tumor suppressor[9]. Several p53 mutants are amyloidogenic in vitro and in vivo[10]. *In vitro* studies have demonstrated that wild-type p53 can form amyloids under specific conditions, including denaturation, acidification, pressure, and high temperature. The presence of p53 aggregates was reported in breast tumors[11],

[1]Departamento de Genética, Instituto de Investigaciones Biológicas Clemente Estable, Montevideo, Uruguay. [2]Sección Bioquímica, Facultad de Ciencias, Universidad de la República, Montevideo, Uruguay. [3]Cátedra de Anatomía Patológica, Hospital de Clínicas, Facultad de Medicina, Universidad de la República, Montevideo, Uruguay. [4]Espacio de Biología Vegetal del Noreste, CENUR Noreste, Universidad de la República, Tacuarembó, Uruguay. [5]Bioterio de roedores, Instituto de Investigaciones Biológicas Clemente Estable, Montevideo, Uruguay. [6]Laboratorio de Biocatalizadores y sus Aplicaciones, Facultad de Ciencias, Universidad de la República, Montevideo, Uruguay. [7]Laboratorio de Inmunovirología, Institut Pasteur de Montevideo, Montevideo, Uruguay. [8]Unidad Académica Inmunobiología, Facultad de Medicina, Universidad de la República, Montevideo, Uruguay. [9]Unidad de Biofísica de Proteínas, Institut Pasteur de Montevideo, Montevideo, Uruguay. [10]Research Technologies, Research Operations and Externalization, GSK-R&D, Boston, USA. [11]Diego Alem and Lucía Canclini contributed equally to this work. ✉email: alemdiego@gmail.com; dalem@iibce.edu.uy; lcanclini@iibce.edu.uy; lcanclini@gmail.com
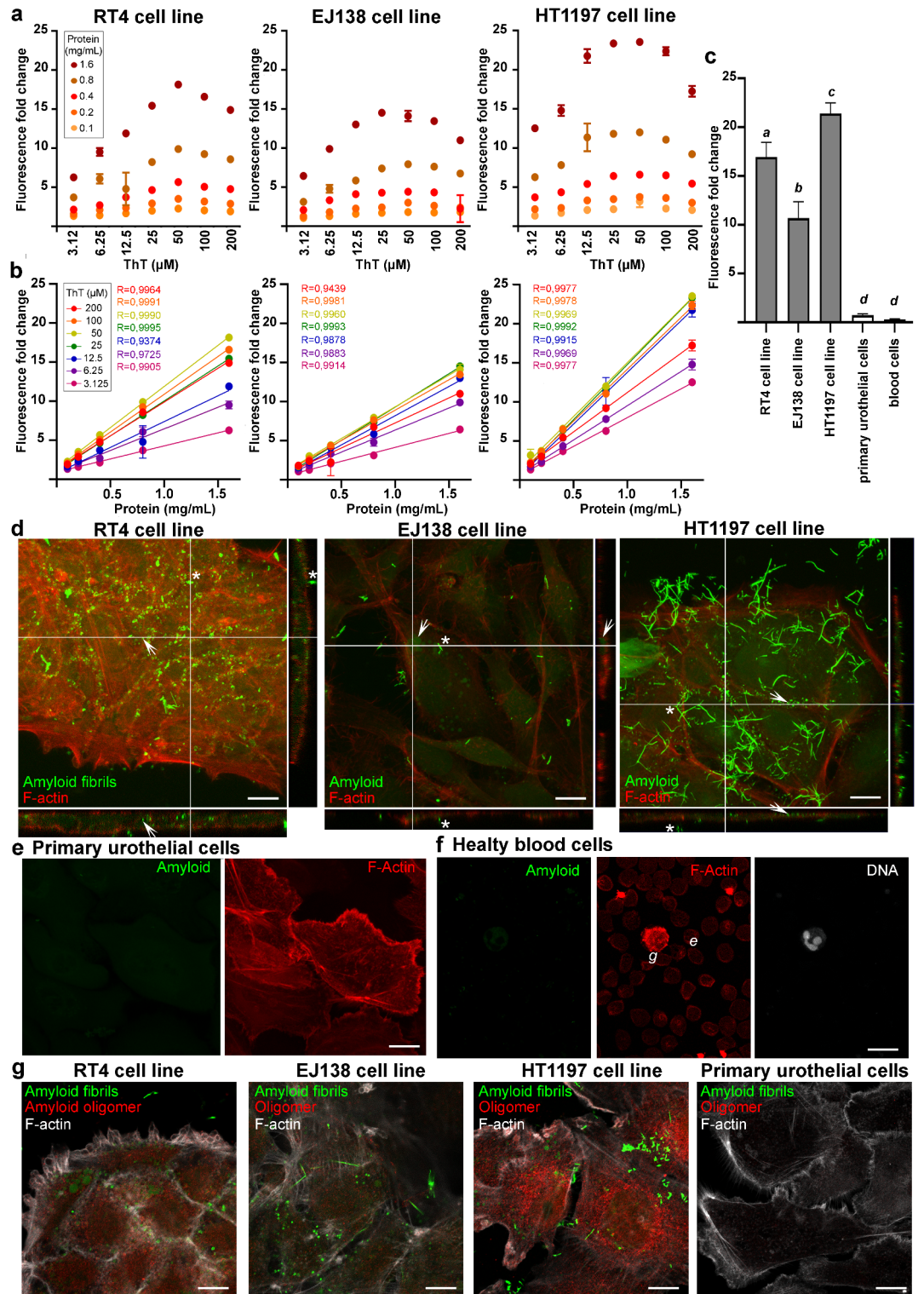
basal cell carcinoma[12], oral and stomach cancer[13], colon cancer and glioblastoma[14]. The loss of p53 function is attributed to the disruption of its native active folding structure. However, the molecular mechanism underlying the gain of function of p53 amyloids remains unresolved[15].

Bladder cancer represents the 10th most prevalent form of cancer worldwide, exhibiting an elevated mortality rate relative to other cancers[16]. Approximately 75% of patients are initially diagnosed with non-muscle-invasive bladder cancer (NMIBC)[17]. After a five-year period, approximately 20% of patients diagnosed with NMIBC will progress to muscle-invasive bladder cancer (MIBC). Patients with MIBC have a lower survival rate than those with NMIBC[18] largely due to the high frequency (approximately 50%) and rapid progression to metastatic cancer[19], which is often incurable. Bladder cancer is highly influenced by environmental factors and life style[20]. The occurrence of mutations in specific genes, including *FGFR*, *TERT*, *RAS*, *KDM6A*, and *TSC1*, has been linked to the carcinogenesis of bladder cancer. Conversely, mutations in p53 and genes associated with DNA damage

◄**Fig. 1**. Determination of amyloid presence in bladder cancer cell lines by spectrofluorimetry (**a**-**c**) and confocal microscopy (**d**-**g**). (**a**) ThT fluorescence fold change (mean ± SD) was plotted *versus* ThT concentration (μM) for serial dilutions (1.6 to 0.1 mg/mL) of protein homogenates from RT4, EJ138 and HT1197 cell lines. The scale of the x-axis is expressed as Log2. (**b**) ThT fluorescence fold change (mean ± SD) was plotted against protein concentration (mg/mL) for ThT serial dilutions (200 to 3.125 μM) for RT4, EJ138 and HT1197 cell lines. (**c**) Spectrofluorometric analysis of ThT (50 μM final concentration) fluorescence fold change of cell homogenates (at 1.6 mg/mL) of each indicated cell type was measured. Letters denote statistical differences between groups. (**d**) RT4, EJ138 and HT1197 cells were stained with ThT (green) to visualize amyloids. F-actin (red) was stained with fluorescent phalloidin to visualize the cell border. Images are representative areas of maximum intensity Z-projections of serial sections at 0.25 μm. Arrows: intracellular/intercellular droplet-like ThT staining. Asterisk: fibril extracellular ThT staining. (**e**) Single focal plane of primary urothelial cells stained with ThT (green) and fluorescent phalloidin (red). (**f**) Single focal plane of blood cells from healthy donors stained with ThT (green), fluorescent phalloidin (red) and TO-PRO-3 iodide (white). g: granulocyte. e: erythrocyte. (**g**) Single focal plane of RT4, EJ138, HT1197 and primary urothelial cells stained with ThT (green), anti-oligomer antibody (red) and fluorescent phalloidin (white) to visualize the cell border. Images shown were taken at identical microscope settings. Bar: 10 μm.

repair have been associated with the progression of NMIBC to MIBC[21]. Considerable effort has gone into classifying bladder cancer samples to enhance comprehension and treatment of the disease[22,23]. Unfortunately, the current classification system still does not enable the prediction of either the progression or recurrence of cancer, nor the prediction of response/resistance to treatments. Despite diagnostic and therapeutic advances, the survival rate of MIBC has remained unchanged over the past 30 years[24], suggesting that some molecular clues have not been considered yet. We hypothesize that amyloids are one of these clues.

In this work, the presence of amyloid in bladder cancer was determined. The characterization of amyloid structures in human bladder cancer cell lines was conducted. Besides, the amyloid proteome of non-invasive and invasive cell lines was determined, in which oncogenes, tumor suppressor proteins and highly expressed tumour-related proteins were found. Moreover, the amyloid proteome exhibited variability between these cell lines, which might be linked to the phenomenon of clonal evolution in which amyloids may play an epigenetic role. Additionally, a chemically induced bladder cancer murine model was developed. In this model, a positive correlation was identified between tumor stage and amyloid content in mice bladders, suggesting a potential association between amyloids and the progression of bladder cancer. Finally, our findings suggest a novel perspective in which gene expression data obtained by transcriptomics/proteomics in cancer should be re-examined.

Results
Characterization of bladder cancer cell lines amyloids
A study was conducted to investigate the presence of amyloid in bladder cancer cell lines derived from tumor tissue at different stages. The cells used in the study were RT4 (grade 1 bladder papilloma cell line, non-invasive)[25], EJ138 (grade 3 bladder carcinoma cell line, invasive)[26], and HT1197 (grade 4 bladder transitional cell carcinoma cell line, invasive)[27]. The determination was made using Thioflavin T (ThT), a widely used fluorescent probe for identifying and analyzing amyloid fibrils in both in vivo and in vitro settings[28]. When bound to amyloid fibrils, ThT displays enhanced fluorescence and a distinctive shift in the absorption/emission spectrum, from 350/438 nm to 450/482 nm[29]. Neither amorphous aggregates nor soluble proteins in folded, unfolded or partially folded states enhance ThT fluorescence[28]. Xue et al. demonstrated that for a given amyloid concentration, the plot of ThT fluorescence fold change (compared to ThT alone) versus ThT concentration shows a bell-shaped curve[30]. A spectrofluorimetric analysis was conducted on homogenates derived from the RT4, EJ138, and HT1197 cell lines, revealing a bell-shaped profile for all three cell lines (Fig. 1a). The maximum fluorescence peak for the three cell lines was observed in the range of 25 to 50 μM of ThT, with HT1197 exhibiting the highest amyloid signal. As previously reported by Xue et al.[30], a linear correlation was observed between ThT fluorescence fold change and amyloid concentration over ThT concentrations ranging from 0.2 to 200 μM. This linear correlation was also apparent in protein homogenates derived from the cell lines (Fig. 1b). The analysis of homogenates of blood cells from healthy donors or primary urothelial cells did not demonstrate the increase in ThT fluorescence that is characteristic of the presence of amyloid (Fig. 1c).

Confocal analysis of ThT-stained cell lines (Fig. 1d) revealed the presence of amyloids fibrils in the cytoplasm and extracellular space of three cell lines, RT4, EJ138 and HT1197. In accordance with the spectrofluorimetry measurements, HT1197 is the cell line with the most pronounced amyloid signal, followed by RT4 and EJ138. In all lines, the intracellular/intercellular staining has a droplet-like punctate appearance, similar to the liquid-liquid phase separation observed in amyloid-β[31], Tau[32] and α-synuclein[33] aggregation during maturation to fibrillary amyloids. Furthermore, extracellular staining with a fibrillar appearance was observed in the three cell lines (see Fig. 1d for Z-projection and Supplementary Fig. 1a, b, c for individual Z-sections). Primary urothelial cells, as well as blood cells from healthy donors did not show staining with ThT (Fig. 1e, f), confirming the absence of amyloids in the latter reported by Lan et al.[34]. The presence of amyloid oligomers in the cytosol of the three tumor cell lines was confirmed by analysis with an anti-oligomer antibody, while no evidence of these structures was found in the primary urothelial cells (Fig. 1g and Supplementary Fig. 2a, b, c, d). Furthermore, the extracellular space was found to be completely devoid of amyloid oligomers. The almost negligible co-localization between amyloid oligomers and amyloid fibrils may reflect the existence of conformational strains in

independent compartments within the cellular environment[35,36]. Therefore, amyloids are not present in normal urothelial cells and could be a molecular marker for bladder cancer.

Amyloids from the cell lines were analyzed by native electrophoresis (Fig. 2a, b). ThT staining of RT4, EJ138 and HT1197 protein homogenates (Fig. 2a) revealed the presence of a ThT-positive smear with a weak fluorescence signal and low mobility, which preceded bands with greater fluorescent intensity and higher electrophoretic mobility. These findings align with the notion that the cellular amyloid population contains amyloids of heterogeneous sizes. Notably, RT4 and EJ138 exhibited similar pattern of bands, while HT1197 showed two additional bands (Fig. 2a). Blood from healthy donors and BSA did not show any ThT staining. Proteinase K digestion of homogenates revealed a unique band in each cell line with a different electrophoretic mobility from that observed prior to protease treatment. Gel filtration of the HT1197 cell line (Fig. 2c) revealed peaks in the ThT fluorescence channel and allowed the apparent size of the HT1197 amyloid bands to be
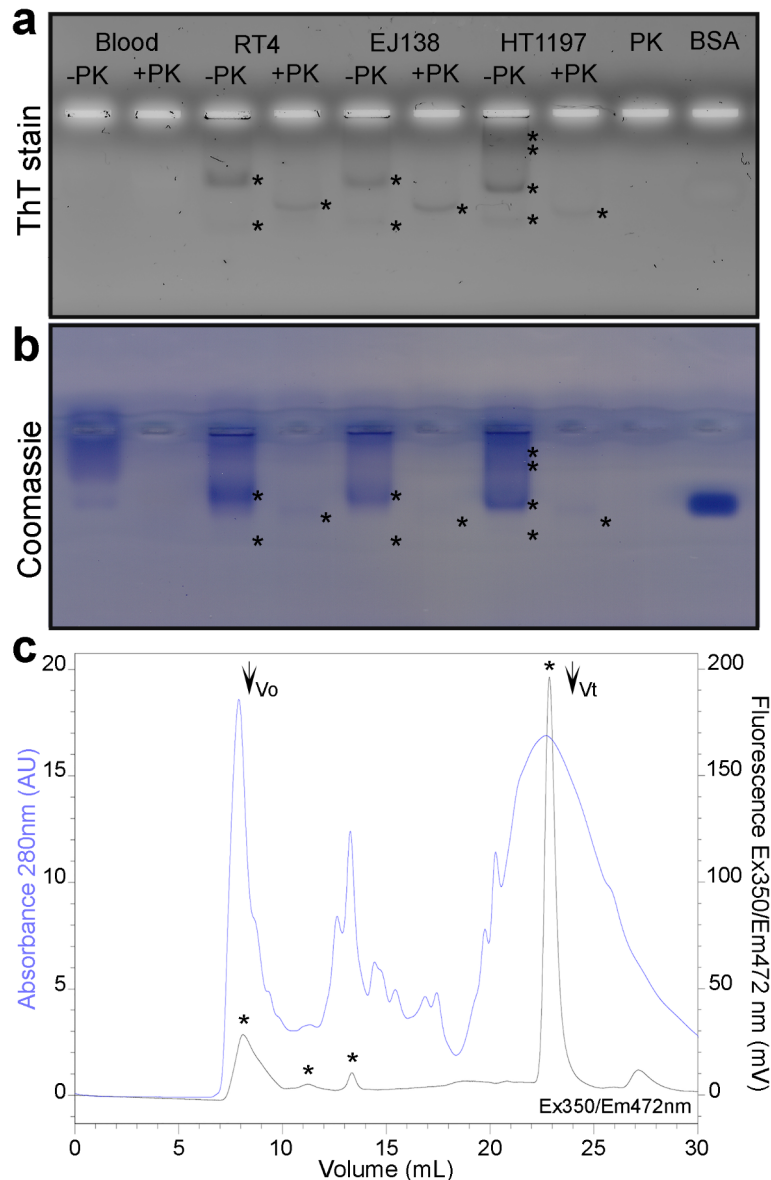

Fig. 2. Electrophoretic and size exclusion chromatographic analyses of cell line amyloids. (**a**) ThT staining of a 1.5% agarose gel native electrophoresis of protein homogenates treated with proteinase K (+ PK) or not treated (-PK). Protein homogenates from blood cells, RT4, EJ138, and HT1197 cell lines were included. The loaded sample in each well is indicated above each lane. Asterisks indicate the presence of positive ThT bands, which appear more evident in the signal on the weaker fluorescent background smear. (**b**) The same gel as in **a**, stained with Coomassie Blue. (**c**) Chromatogram obtained during gel filtration of HT1197 protein homogenate mixed with ThT, using Superdex matrix 200 (range: 3-600 kDa), recorded with in-line PDA (absorbance at 280 nm, 10^{-3} AU, blue line) and FD (Ex350 nm and Em472 nm, mV, black line). X-axis is elution volume (mL). Arrows indicate void volume (Vo) and total volume (Vt). Asterisks indicate ThT-positive peaks.

estimated as > 670 kDa, 215 kDa, 74 kDa, and < 10 kDa. Gel filtration analysis of amyloid fibrils, either produced in vitro or purified from natural sources, showed patterns similar to those found in our experiments[37].

Identification of amyloid proteome from bladder cancer cells

The first step in the identification of the amyloid proteins was their purification. Purified amyloids were obtained as described in Materials and Methods. Confocal microscopy analysis showed the characteristic ThT staining signal of amyloids (Fig. 3a), whereas blood samples subjected to the same purification protocol and stained with ThT showed no signal. Transmitted electron microscopy of negatively stained EJ138 and HT1197 (Fig. 3a) purified pellet revealed the presence of amyloid fibrils, consistent with previous findings in amyloids purified from Alzheimer's brains[38]. Blood from healthy donors led to the purification of particulate material without amyloid appearance. RT4 negatively stained pellet also showed fibrillary amyloids, but embedded in an amorphous aggregate (Fig. 3a) already described in vitro[39]. Blood from healthy donors led to the purification of particulate material without amyloid appearance. Purified amyloids were also stained with Congo red and observed under a polarized microscope, where the typical green apple birefringence of Congo red in the presence of amyloids could be observed (Fig. 3a). Conversely, despite the presence of certain particles collected from the ultracentrifugation of blood from healthy donors, which appeared red, no birefringence was observed (Fig. 3a). Collectively, the microscopic analysis of ultracentrifuged pellets of bladder cancer cell lines demonstrated that amyloids were successfully recovered from cancer cell lines. It is worth noting that part of the purified pellets from all three cell lines could not be resuspended at all, showing the aggregation in more insoluble forms due to the increase in amyloid concentration after centrifugation. To confirm the amyloid nature of the proteins obtained from the bladder cancer cell lines by ultracentrifugation, we performed far-UV circular dichroism (CD) analyses (Fig. 3b). In order to circumvent the potential interference of contaminants on the CD spectra, the homogenates were treated with proteinase K prior to ultracentrifugation. The samples from the EJ138 and HT1197 cell lines exhibited a spectrum in accordance with reported amyloid structures[40–42]. The data analysis for secondary structure estimation revealed that the samples contain no α-helix and a β-sheet content of 34.2% and 35.5%, respectively. These findings are consistent with those reported in the literature[42,43]. It is noteworthy that the signal for HT1197 was weak due to the effects of fibril sedimentation. The complete characterization of amyloids from the RT4 cell line via CD proved challenging due to the native heterogeneity and fibril sedimentation of the samples, which resulted in a greater reduction in the soluble protein concentration than was observed for the HT1197 samples. To gain further insight into the amyloid characterization, the samples were subjected to centrifugation, and complementary analyses were conducted using Dynamic Light Scattering (DLS) to determine the size of the supernatant proteins. The soluble amyloids from these cell lines exhibited variable hydrodynamic radii (RH), with values ranging from 20 to 100 nm (Fig. 3c). Size distributions of EJ138 and HT1197 amyloids were polydisperse and multimodal, with larger sizes, whereas RT4 amyloids exhibited monodisperse behavior with smaller sizes. Additionally, the thermal stability of these samples was evaluated using nanoDSF as previously described[44]. As anticipated for amyloid proteins, no thermal transitions were observed during heating and cooling scans (Fig. 3d).

Two cell lines were selected for further analysis of the derived amyloids: the non-invasive RT4 and the invasive HT1197. Purified amyloids from RT4 and HT1197 were subjected to mass spectrometry (MS) following proteinase K treatment to minimize the likelihood of identifying contaminants that might co-purify with them[45]. Nearly 2000 proteins were identified in protease-resistant samples obtained after ultracentrifugation (Supplementary Table 1). KEGG pathway enrichment analysis revealed the presence of proteins associated with the proteasome and amyloid-related neurodegenerative diseases in the first groups represented (Supplementary Table 1). Nevertheless, the majority of ribosomal proteins were also identified, which suggest the potential presence of ribosomal contamination in amyloid purifications. Given that ribosomes can be recovered on sucrose gradients and may be partially resistant to proteases[46,47], we sought to further avoid putative contaminants in the MS-derived list by taking advantage of the solubilization resistance of amyloids[48–50]. To this end, a differential proteomic analysis was performed between amyloids solubilized in formic acid and those treated with water. The resulting list contain 184 enriched proteins in formic acid for the RT4 cell line (Supplementary Table 2), for which the most represented protein was PGK1 (fold change = 66.8, $p = 0.02$). PGK1 is also a mutated gene in this cell line (Supplementary Table 2). In HT1197, MS analysis identified 59 proteins (Supplementary Table 2), for which the most represented protein was HDAC1 (fold change = 7.1, $p = 0.0007$). Mutant proteins in both cell lines were identified as constituents of amyloid. In addition to PGK1, as previously mentioned, the TRMT61A protein, whose gene carries a point mutation, was identified in the RT4-derived amyloids. Furthermore, in HT1197, two proteins whose genes carry point mutations (GNB2 and ARFGEF2) were also found in amyloids derived from the HT1197 cell line (Supplementary Table 2).

Since proteinase K is a nonspecific protease, we expected to recover those peptides that were protected by being hidden in the super-resistant amyloid structure. To verify this, we performed a prediction analysis of prone-aggregation regions for the first five proteins in each list and compared how many peptides identified in each case corresponded to these regions (Fig. 4a and Supplementary Information Data). Most peptides contain an amyloidogenic region, supporting that these lists contain the amyloid proteome of each cell line. We did not observe this behavior for those proteins found by MS that were not enriched in the formic acid *versus* water differential analysis (Supplementary Information Data). These examples include housekeeping proteins that probably survive proteolysis due to their high expression level, and for which virtually all peptides identifiable by MS were identified, regardless of their aggregation capacity.

A KEGG Mapper analysis revealed that amyloids contain proteins from molecular networks including cancer-related pathways, viral carcinogenesis, PI3K/Akt signaling pathway, Ras signaling pathway and cell cycle (Fig. 4b, c). We highlight, in RT4 amyloids, the presence of proteins related to amyloid-related neurodegenerative diseases (Fig. 4b).

a. Microscopic analysis
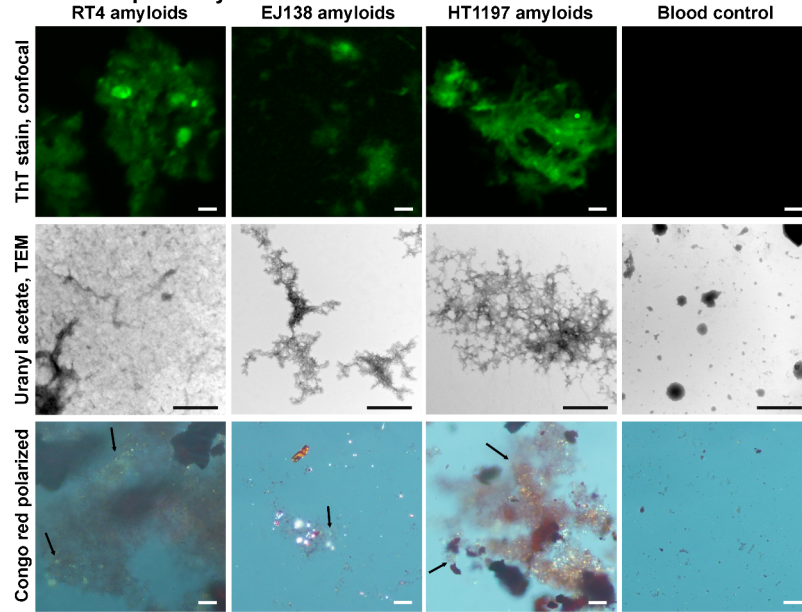
b. Far-UV CD analysis
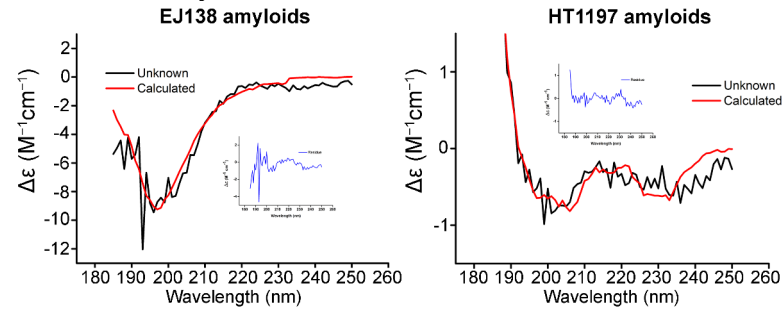
c. Dynamic Light Scattering
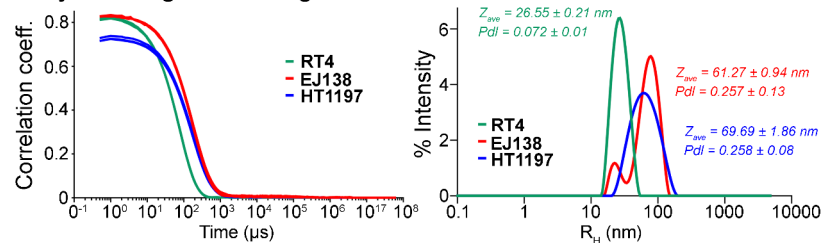
d. Differential Scanning Fluorimetry
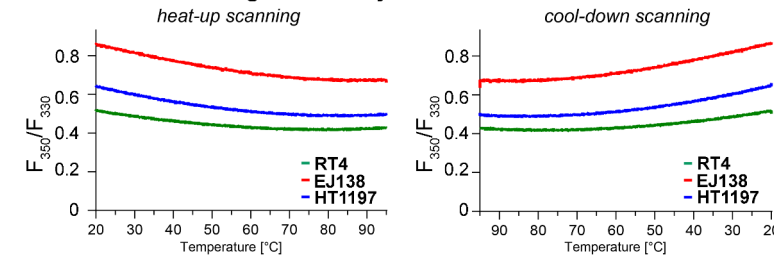
Fifteen proteins are shared between the amyloid proteomes of both cell lines (Fig. 4d, e and Supplementary Table 2). Analysis of the overlap between the RT4 and HT1197 amyloid protein datasets reveals the presence of cancer-related proteins (Fig. 4d, e), in particular the tumor suppressor/oncogene HDAC1 and the bladder cancer driver RhoA. Furthermore, the presence of these two proteins was confirmed by dot blot analysis of the isolated amyloid fractions. As illustrated in Fig. 4f, the anti-HDAC1 and anti-RhoA antibody signals were observed in both amyloid purifications after formic acid treatment, indicating that the epitopes are hidden in the amyloid structure. The blots in their original state are presented in Supplementary Fig. 3.

The proteins with the highest difference in solubility in formic acid were selected to confirm their presence in aggregates: PGK1 for RT4 and HDAC1 for HT1197. We also investigate the subcellular distribution of the bladder cancer driver RhoA, which is common to the identified amyloid proteins from both cell lines. As the amyloid structure can mask epitopes of the proteins, we included a strong formic acid treatment to unmask

◀ **Fig. 3**. Analysis of cell line amyloids purified by ultracentrifugation. (**a**) Microscopic analysis of purified amyloids from RT4, EJ138 and HT1197, stained with ThT and visualized by fluorescence microscopy, Congo red and visualized by polarization microscopy or uranyl acetate and visualized by transmitted electron microscopy. The arrows in each image show examples of the green-yellow colour of the amyloids when they are stained with Congo red and observed under polarized light. Blood samples from healthy donors subjected to the same ultracentrifugation protocol were included as a negative control for each staining. Bars: 1 μm. (**b**) Far-UV CD analysis of amyloids derived from EJ138 and HT1197. The black line represents the data obtained, while the red trace corresponds to the best fit from the analysis performed with the BeStSel web server (https://bestsel.elte.hu/), which indicates that EJ138 and HT1197 have β-sheet contents of 34.2% and 35.5%, respectively. The inset shows the residuals of the fit. (**c**) Dynamic Light Scattering (DLS) analysis of amyloids derived from RT4, EJ138 and HT1197 cell lines. The left panel illustrates the highly reproducible autocorrelation functions obtained in triplicate for each batch, while the right panel depicts representative intensity-weighted size distributions. The hydrodynamic radius (RH) is plotted on the x-axis, and the Z-average (Zave) and polydispersity index (PdI), calculated as the mean of three replicates, are indicated alongside each distribution. (**d**) Differential Scanning Fluorimetry (DSF) obtained with amyloids from RT4, EJ138 and HT1197 cell lines. The ratio of intrinsic fluorescence measured at 350 and 330 nm upon heating and cooling scans is displayed in the left and right panels, respectively.

them[51] and compare the distribution of each protein before and after antigen retrieval. F-actin staining with fluorescent phalloidin was included to confirm the efficiency of the formic acid treatment. Because ThT binds to highly ordered amyloid structures, where antibody-recognized epitopes may be masked, we do not expect a high degree of co-localization between ThT and antibody signals. However, staining with ThT was included to corroborate the partial solubilization of amyloids with formic acid treatment (Fig. 5).
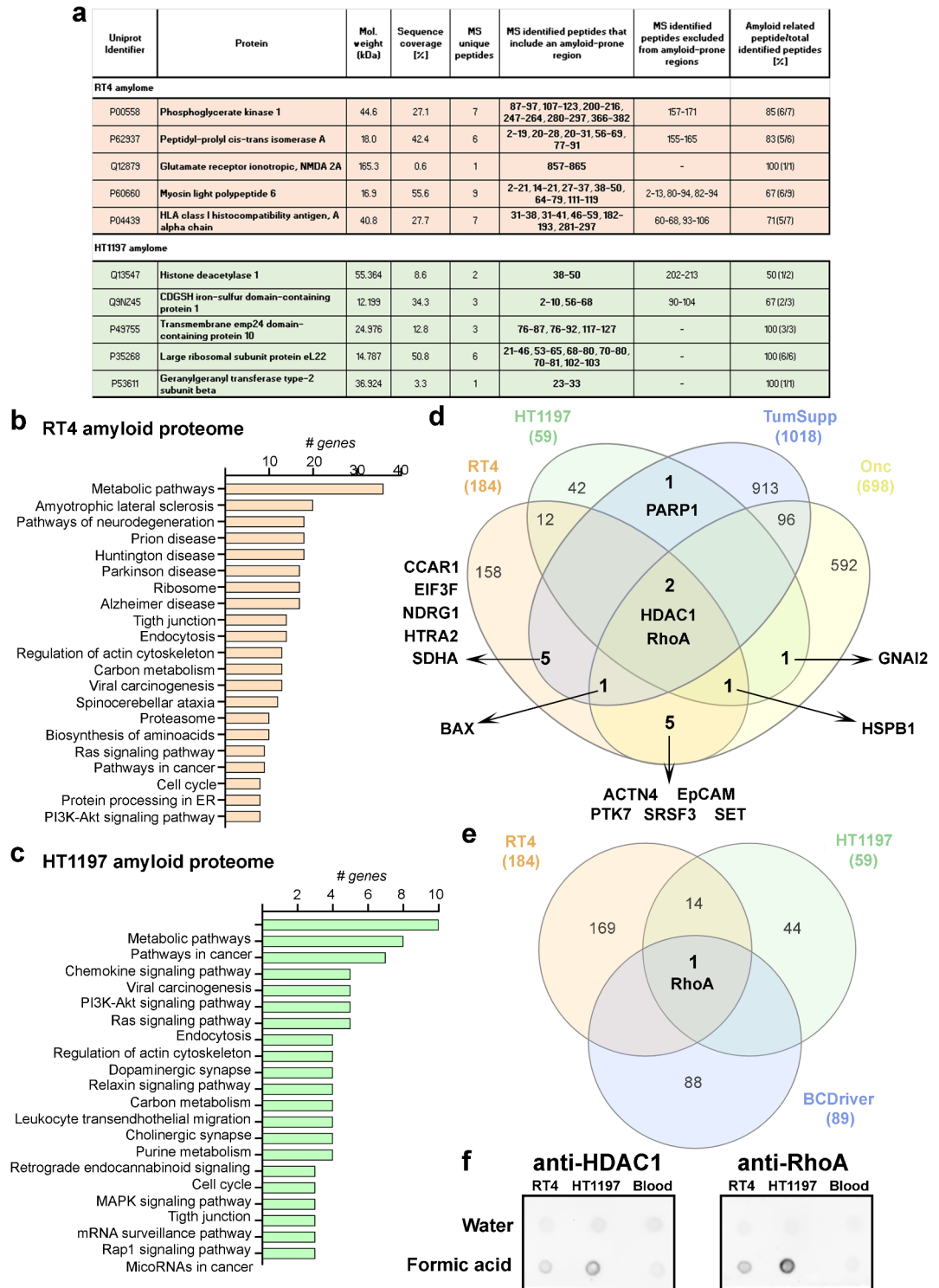
A punctate cytoplasmic and nuclear signal for the anti-PGK1 antibody was observed in both RT4 and HT1197 cell lines without formic acid treatment (Fig. 5a, red channel, Supplementary Fig. 4a). After antigen retrieval, the F-actin signal disappeared (Fig. 5a, white channel), demonstrating that soluble proteins are not resistant to formic acid. On the other hand, the ThT signal remained after unmasking treatment, although with a different appearance, demonstrating that 70% formic acid is enough to change the conformation of the RT4 and HT1197 amyloids, partially dissolving them and thus unmasking hidden epitopes. Regarding the PGK1 signal on RT4 cells, its punctate distribution changes after 70% formic acid to a stronger signal at the cell border (Fig. 5a, red channel), confirming the highly packaged state of most PGK1. This agreed with the identification of PGK1 by MS analysis in the RT4 amyloid proteome. Interestingly, we did not detect any PGK1 signal in HT1197 cells treated with formic acid (Fig. 5a, red channel), confirming that this protein is not folded into an amyloid structure in this cell line.

HDAC1 is the protein with the highest fold change in HT1197 MS amyloid proteome (Supplementary Table 2), and showed an intracellular punctate signal in non-formic acid-treated cells (Fig. 5b, red channel, Supplementary Fig. 4b). On the other hand, RT4 showed an almost exclusively pan-nuclear punctate distribution of HDAC1 before formic acid treatment (Fig. 5b, nuclei, red channel, Supplementary Fig. 4b). In both cell lines without formic acid treatment, a fibrillar signal of HDAC1 was also observed, coinciding with the extracellular fribrillary ThT signal distribution (Fig. 5b, arrows, red channel). Antigen retrieval revealed a stronger signal from the anti-HDAC1 antibody in the cytoplasm of HT1197 cells (Fig. 5b, asterisk, red channel), while the extracellular fibrillary signal remained visible (Fig. 5b, arrowhead, red channel), supporting the amyloid structure of HDAC1 suggested by the MS data. In RT4 cells, the HDAC1 signal remains in an extracellular fibrillary distribution following formic acid treatment. As previously described, however, the HDAC1 signal is evident in the nuclei prior to the unmasking treatment. Although extracellular amyloids sequestered HDAC1 proteins, an important fraction of soluble HDAC1 is present in RT4 cells. This finding is consistent with the MS data, where the HDAC1 fold change between formic acid-solubilized and non-solubilized samples in RT4 was close to the threshold (fold change = 2.8; Supplementary Table 2).

Immunocytochemical analysis for RhoA revealed the presence of a faint punctate intracellular signal in both cell lines that had not been treated with formic acid (Fig. 5c, red channel). Moreover, some fibrillar distribution was observed in HT1197 cells (Fig. 5c, arrows, green and red channels). The treatment of RT4 cells with formic acid resulted in an enhancement of the RhoA signal, which lends support to the proposition that it should be included on an amyloid. It is noteworthy that the distribution of RhoA after formic acid treatment exhibited a similar pattern to that observed for PGK1, with a cytoplasmic distribution at cell borders (Fig. 5a). In HT1197, there was no increase in RhoA signal intensity. The formic acid treatment resulted in the persistence of a punctate low signal within the cytoplasm, suggesting the possibility of integration of some RhoA molecules into an amyloid structure.

Analysis of amyloids in an in vivo model of bladder cancer

The presence of amyloid in bladder cancer was also investigated in a murine bladder cancer model generated by the administration of BBN for either 16 or 23 weeks (Supplementary Fig. 5a). After 16 weeks, all treated mice (*n* = 16) exhibited lesions. The histological analysis revealed that 37.50% of the mice exhibited dysplasia, 56.25% had carcinoma in situ (CIS), and 6.25% had invasive carcinoma (Supplementary Fig. 5b, c). At 23 weeks, 7.20% of mice still exhibited CIS (*n* = 1), 21.40% developed invasive carcinoma confined to the lamina propria (*n* = 3), and 71.40% developed invasive carcinoma of the muscularis propria (*n* = 10) (Supplementary Fig. 5b, c). Control non-BBN-treated mice exhibited normal bladders at both 16 and 23 weeks.

a

Uniprot Identifier	Protein	Mol. weight (kDa)	Sequence coverage [%]	MS unique peptides	MS identified peptides that include an amyloid-prone region	MS identified peptides excluded from amyloid-prone regions	Amyloid related peptide/total identified peptides [%]
RT4 amylome							
P00558	Phosphoglycerate kinase 1	44.6	27.1	7	87–97, 107–123, 200–216, 247–264, 280–297, 366–382	157–171	85 (6/7)
P62937	Peptidyl-prolyl cis-trans isomerase A	18.0	42.4	6	2–19, 20–28, 20–31, 56–69, 77–91	155–165	83 (5/6)
Q12879	Glutamate receptor ionotropic, NMDA 2A	165.3	0.6	1	857–865	–	100 (1/1)
P60660	Myosin light polypeptide 6	16.9	55.6	9	2–21, 14–21, 27–37, 38–50, 64–79, 111–119	2–13, 80–94, 82–94	67 (6/9)
P04439	HLA class I histocompatibility antigen, A alpha chain	40.8	27.7	7	31–38, 31–41, 46–59, 182–193, 281–297	60–68, 93–106	71 (5/7)
HT1197 amylome							
Q13547	Histone deacetylase 1	55.364	8.6	2	38–50	202–213	50 (1/2)
Q9NZ45	CDGSH iron-sulfur domain-containing protein 1	12.199	34.3	3	2–10, 56–68	90–104	67 (2/3)
P49755	Transmembrane emp24 domain-containing protein 10	24.976	12.8	3	76–87, 76–92, 117–127	–	100 (3/3)
P35268	Large ribosomal subunit protein eL22	14.787	50.8	6	21–46, 53–65, 68–80, 70–80, 70–81, 102–103	–	100 (6/6)
P53611	Geranylgeranyl transferase type-2 subunit beta	36.924	3.3	1	23–33	–	100 (1/1)

b RT4 amyloid proteome

c HT1197 amyloid proteome

d

e

f anti-HDAC1   anti-RhoA

Spectrofluorimetric analysis of healthy (water-treated) mouse bladder homogenates using ThT revealed no significant differences in basal ThT fluorescence between 16 and 23 weeks (Fig. 6a, $p = 0.9997$). At 16 weeks, a slight trend (not statistically significant) towards increased ThT fluorescence was observed in BBN-treated mice compared to their control counterparts (Fig. 6a, $p = 0.5563$). After 23 weeks of BBN treatment, bladder homogenates exhibited elevated ThT fluorescence levels in comparison to control bladders (Fig. 6a, $p = 0.0134$). A strong positive correlation was observed between the ThT fluorescence of bladder homogenates and the stage of bladder cancer as determined by spectrofluorimetry (Fig. 6b, $r = 0.722$, $p < 0.0001$). The quantification of ThT-stained mouse bladder slides observed at low magnification by confocal microscopy yielded comparable results, with statistically significant differences between BBN-treated and control mice at 23 weeks ($p = 0.0333$, Supplementary Fig. 6a, b, c). Additionally, a positive correlation was observed between ThT fluorescence and bladder cancer stage, as determined by confocal microscopy ($r = 0.7672$, $p < 0.0001$, Supplementary Fig. 6b). At low magnification (Fig. 6c-f), ThT is able to distinguish between normal and pathological bladders. In the case of

◀ **Fig. 4**. Determination of amyloid proteome of RT4 and HT1197 cell lines. (**a**) Aggregation-prone analysis of the first MS-identified proteins for each cell line. Identifiers, name, and molecular weights of identified proteins are indicated, as well as the number of identified peptides and the sequence coverage of each protein. MS-identified-peptides containing amyloid-prone regions are indicated in bold letters, also related to no amyloid-prone identified peptides by percentages. (**b,c**) KEGG Mapper analysis of amyloid proteins in RT4 (**b**) and HT1197 (**c**). Pathways are depicted by decreasing number of genes in each one. (**d**) Venn diagram showing the overlap between amyloid-identified proteins of RT4 and HT1197 cell lines and tumor suppressor (TumSupp) and/or oncogenes (Onc). Numbers in parentheses indicate the total number of elements in each set. Protein identity for elements in selected overlaps is indicated. (**e**) Venn diagram showing the overlap between amyloid-identified proteins of RT4 and HT1197 cell lines and bladder cancer driver genes (BCDriver). Numbers in parentheses indicate the total number of elements in each set. (**f**) Dot blot analysis with anti-HDAC1 and anti-RhoA antibodies on purified amyloids derived from RT4 and HT1197 cells. Prior to being spotted on the membrane, the purified amyloids were dissolved in either water or formic acid, as indicated. Blood was included as a control. The images of the blots were subjected to cropping in order to enhance clarity. The blots in their original state are presented in Supplementary Fig. 3.

the normal bladder (Fig. 6c), the signal was absent. In contrast, in CIS (Fig. 6d), the signal was restricted to the urothelium. In more advanced stages (Fig. 6e, f), the signal was observed to invade the underlying tissues. In the mice with high ThT signal, ThT was distributed throughout the bladder tissue (Fig. 6f). At high magnification (63x, Fig. 6g-j), amyloid was observed in the cytoplasm of cells at all stages. Additionally, nuclear (Fig. 6i, j) and extracellular amyloid deposition (Fig. 6j) were observed in invasive carcinoma of the muscularis propria.

Discussion

Tumorigenesis is a multifactorial process involving both genetic alterations and environmental events that contributes to the development of cancer. Genetic alterations can affect the genome of cells, leading to transformation and the selection of those cells with growth advantages[52,53]. Driver mutations result in the activation of proto-oncogenes or the inactivation of tumor suppressors[54] in the original tumor cells. The progeny of these cells are then selected through a combination of the acquisition of new mutations[55] and the pressure exerted by the tumor environment[56–58], which results in cancer progression. Thus, cancer can be conceptualized as an evolving population where its individuals undergo speciation and diversification[59] through a learning process involving adaptive evolution. It has been proposed that this evolvability is based on epigenetic mechanisms, such as cellular stress and chromatin remodeling[60]. We suggest that amyloids represent an unexplored epigenetic mechanism that may also provide an explanation for evolvability.

Amyloids have been demonstrated in breast cancer[11,61], basal cell carcinoma[12] and gastric cancer[13], where the authors showed co-localization of p53 with anti-amyloid antibodies signal. In a recent article, Farris et al. reported the secretion of amyloids by melanoma and pancreatic ductal adenocarcinoma cells[42]. Here, we demonstrated the presence of amyloid in three human bladder cancer cell lines. Additionally, an in vivo model of bladder cancer was generated using BBN, a compound found in tobacco smoke that induces lesions in murine bladders similar to those observed in human bladder cancer[62,63]. The protocol employed herein models all stages of bladder cancer, thereby approximating the complexity of a natural cancer. Furthermore, the in vivo model demonstrates the presence of amyloids, expanding the range of neoplasms in which amyloid has been reported.

Our results suggest that the amyloid proteome is complex, comprising dozens of proteins that are packaged in a protease-resistant form. The complexity of the amyloid proteome[64] is a concept that has been discussed in the context of Alzheimer[65–67] and Parkinson[68] diseases, two neuropathological disorders classically recognized as being caused by amyloids. In addition to the protease-resistant fraction, bladder cancer amyloids are composed of a protein fraction that is not resistant to these enzymes, as demonstrated by native electrophoretic analysis. It remains to be seen whether this fraction consists of the flanking regions of the amyloid core-forming sequences[69] or of proteins sequestered within the amyloid[70]. A question that will be addressed in the future.

The formation of pathological amyloids is a consequence of the alteration of protein folding in regions that are prone to amyloidogenesis as a result of genetic mutations, overexpression, and/or aberrant proteolytic cleavage[71]. Genetic mutations that promote aggregation can occur in the core segment itself or in flanking regions of the fibril-forming peptide[72]. Among the proteins we identified in the amyloids of bladder cancer cell lines, mutant proteins were found. The question of whether these mutant proteins are responsible for the formation of the amyloid core will be addressed in future research.

PGK1 plays a crucial role in ATP generation during glycolysis. A point mutation (Q300K) has been identified in PGK1, and its overexpression has been observed in RT4 cells[73]. Studies of PGK1 deficiency syndrome, a rare X-linked metabolic disorder, have shown that this is a conformational disease based on the aggregation propensity of PGK1 mutants[74,75]. It is noteworthy that PGK1 has also been linked to amyloid-related neuropathies. PGK1 was found in amyloid plaques in Alzheimer disease[76]. In Parkinson disease, PGK1 is upregulated[77]. In this disease, while the activity of the protein has been shown to be reduced by point mutations[78–81], the effect of which on folding has not been described[82]. PGK1 variants with altered kinetics and thermodynamic stability have been reported in cancer[83]. PGK1 gene expression is negatively correlated with prognosis in most cancers, with overexpression correlating with poor patient survival[84]. Many oncogenic functions of PGK1 have been explained by demonstrating an increase in its function, but most have looked only at its expression level, and many controversial data have been collected on the relationship between PGK1 expression level and its oncogenic or tumor suppressor behavior[85]. Whether overexpression of PGK1 leads to its fibrillation into an
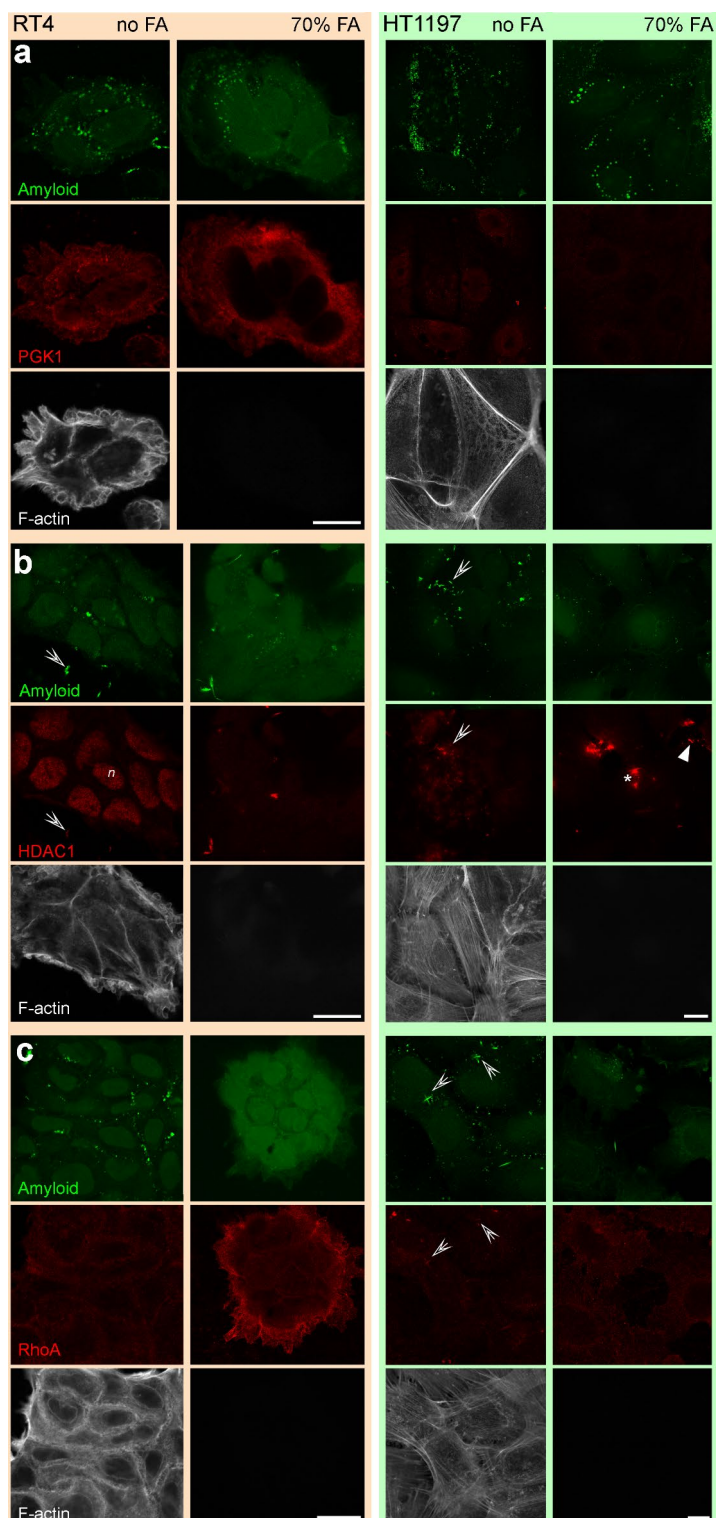
Fig. 5. PGK1 (**a**), HDAC1 (**b**) and RhoA (**c**) distribution in RT4 and HT1197 cells. Images are single focal planes at intracellular level of immunocytochemistry experiments showing the distribution of each protein antibody signal (red) on RT4 and HT1197 cells treated or not treated with 70% formic acid. ThT (green) and fluorescent phalloidin (white) were included as counterstain probes. Arrows: extracellular fibrillar signal; arrowhead: extracellular fibrillary signal in FA treated cells; asterisk: intracellular signal in FA treated cells. Bar: 10 µm.
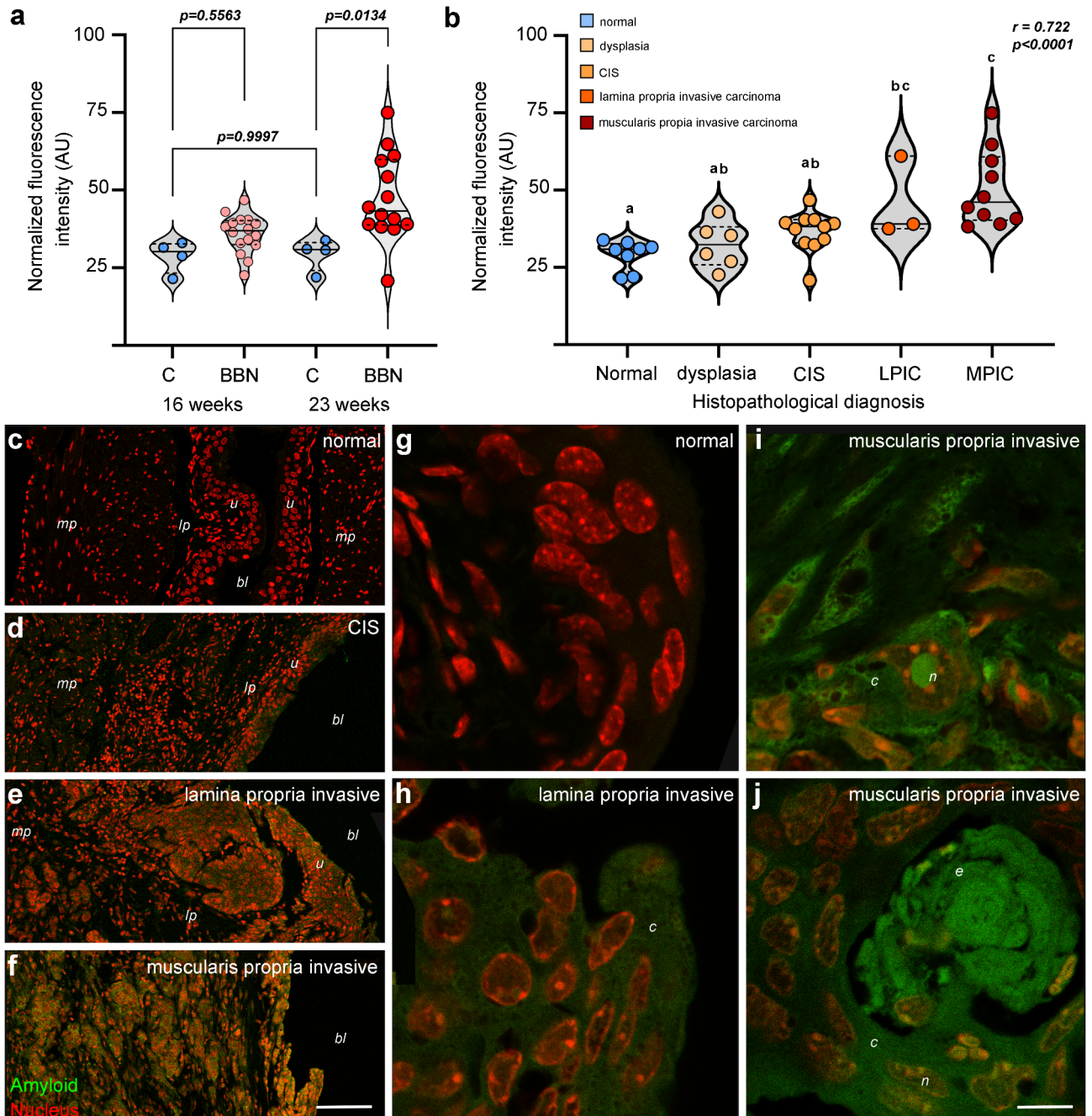
Fig. 6. Detection of amyloids in mouse bladder tumors. (**a**) Normalized ThT fluorescence intensity measured by spectrofluorimetry of bladder homogenates. Control (C) and BBN-treated mice at 16 or 23 weeks are compared. *p-value* between groups is indicated. (**b**) Correlation graph between normalized ThT fluorescence intensity and observed histological changes. ThT fluorescence intensity was measured by spectrofluorimetry of bladder homogenates from control (C) or BBN-treated mice at 16 or 23 weeks. LPIC: lamina propria invasive carcinoma; MPIC: muscularis propria invasive carcinoma. ANOVA linear correlation coefficient and *p-value* are shown. (**c**–**f**) Focal planes of bladder sections stained with ThT (green) and TO-PRO-3 iodide (red) at 10x magnification. Histopathological diagnosis is indicated. bl: bladder lumen; u: urothelium; lp: lamina propria; mp: muscularis propria. Bar: 100 μm. (**g**–**j**) Focal planes of bladder section stained with ThT (green) and TO-PRO-3 iodide (red) at 63x magnification. Histopathological diagnosis is indicated. c: cytoplasm; n: nucleus; e: extracellular. Bar: 10 μm.

amyloid and the consequent loss of its function is a fact that has escaped the scrutiny of cancer researchers and should be a focus of future attention.

The oncogene/tumor suppressor duality is a feature also shared by HDAC1 and RhoA[86]. HDAC1 is a component of the SIN3A, NuRD and CoREST transcriptional complexes, which are recruited to promoters

by DNA binding proteins to induce gene-specific transcriptional silencing[87]. Although HDAC1 knockout/inhibition experiments have generally shown a decrease in cell proliferation[87], HDAC1 has also been reported to exert oncogenic functions depending on tumor type, microenvironment and stage[88]. In bladder cancer, HDAC1 also shows patient-dependent mutations and expression levels[87], and its silencing results in a cell line-dependent response, with some cell types dying and other unresponsive even at high initial HDAC1 expression levels[89]. None of the cell lines tested by the authors match those in this study, and we cannot know whether the lack of response they found is due to HDAC1 folding into an amyloid. RhoA is a small GTPase that plays a role in migration, adhesion, proliferation and gene expression[90]. The function of RhoA in cellular migration and adhesion is dynamic, changing from stress fibers to lamellae formation in a balance between RhoA activation, subcellular localization and interactions with downstream effectors[91]. Several RhoA mutations found in cancer lead to gain-of-function changes in an unidentified signaling pathway[92], which could be an amyloidogenic-dependent pathway. In addition, RhoA knockdown inhibits cancer cell migration and invasion[93–95]. According to the differences we found in the amyloid sequestering degree of RhoA between RT4 and HT1197, it will be interesting to study in the future if this could explain the high difference in the migratory capacity of both cell lines[96].

The accumulation of mutations caused by the genomic instability inherent in tumorigenesis may lead to the selection of mutations in key genes for amyloid formation. Analysis of the common amyloid proteome between cell lines derived from different tumors may provide useful data in this regard. Comparing the amyloid proteome of the cell lines studied in this paper with that of the recently published paper by Farris et al.[42], we found four proteins common to all cell lines. Interestingly, two of these are members of the 14-3-3 protein family. These small, highly conserved proteins are involved in cell survival, differentiation, migration, apoptosis and have recently been shown to form amyloid[97]. Despite some common proteins, the amyloid proteome is variable between cancer cell lines, which may be related to tumor clonal evolution, where amyloids represent an epigenetic form of evolvability[98]. Whether differential amyloid proteins between different tumor grades may be related to the acquisition of more aggressive phenotypes will be the subject of more detailed future research. For now, we find a positive correlation between tumor stage and amyloid content in an in vivo murine bladder cancer model, demonstrating that amyloids are associated with cancer progression. That amyloids have been linked to invasiveness, metastasis and even drug resistance[10,99] opening up an interesting perspective for exploring new therapeutic avenues.

Finally, our findings open a new vision in which the presence of increased expression of an mRNA or protein in cancer may not necessarily be related to increased function. In this new paradigm, in which amyloids could act as traps that sequester proteins, gene expression data obtained by transcriptomics/proteomics and protein-protein interaction data found by immunoprecipitation in cancer should be re-examined.

Materials and methods
Ethics declarations
Human procedures were performed in accordance with the Uruguayan legislation regarding the use of human samples (National Laws #18331 and #18335, Presidential Decrees #001-4573/2007, #274 – 010, #158 – 019 and #414–2009, and Ministry of Health Regulation #827) and were approved by the IIBCE Human Research Ethics Committee. Informed consent was obtained from all subjects.

Animal procedures were performed in accordance with the guidelines of the National Commission for Animal Experimentation (CNEA), the Uruguayan Law on the Care and Use of Laboratory Animals, and in accordance with ARRIVE guidelines. The specific protocol was approved by the Animal Use Ethics Committee CEUA-IIBCE (protocol number 001/10/2020).

Human cell lines and blood samples
RT4 (ECACC 91091914), EJ138 (ECACC 85061108) and HT1197 (ECACC 87032403) cell lines were obtained from the European Collection of Authenticated Cell Cultures (ECCAC). Human primary bladder epithelial cells were obtained from the American Type Culture Collection (ATCC). RT4 cells were maintained in McCoy's 5 A medium (M4892, Sigma-Aldrich) supplemented with 10% FBS (FBS-11A, Capricorn). EJ138 and HT1197 cell lines were maintained in EMEM medium (M0643, Sigma-Aldrich) supplemented with 10% FBS. Primary bladder epithelial cells (healthy 33-year-old male) were maintained in bladder epithelial cell basal medium (PCS-420-032, ATCC) supplemented with 5 µg/mL apotransferrin, 1.0 µM adrenaline, 0.4% extract P, 100 ng/mL hydrocortisone hemisuccinate, 6 mM L-glutamine, 5 µg/mL human recombinant insulin, 5 ng/mL human recombinant EGF, 0.5 ng/mL human recombinant TGF-α and 5 ng/mL human recombinant KGF (all included in the Bladder Epithelial Cell Growth Kit, PCS-420-042, ATCC).

Blood samples from healthy donors were obtained by peripheral venipuncture and collected in 1 mL blood collection tubes (Vacuette tubes, #454034, Greiner Bio-One). Blood samples were immediately processed for confocal microscopy or preparation of protein homogenates.

Murine bladder cancer model
Four-week-old male C57BL/6J mice (The Jackson Laboratory, USA) were obtained from the Transgenic and Experimental Animal Unit of the Instituto Pasteur Montevideo (IPMont, Montevideo, Uruguay). After one week of acclimatization, the mice were randomly divided into two groups: a control group and a group treated with N-butyl-N-(4-hydroxybutyl)-nitrosamine (BBN) (Supplementary Fig. 3a). BBN (AG003T8T, Angene) was administered at 0.05% in the drinking water (*ad libitum*). After 16 or 23 weeks, mice were sacrificed by cervical dislocation. Bladders were harvested and divided into two halves. One half was immediately fixed in 4% formalin. The other half was kept in liquid nitrogen for further protein extraction.

Histopathological assessment of bladder lesions

Fixed bladders were extensively washed with PBS 1X, pH7.4 and embedded in paraffin by serial passages through ethanol 96% (2×30 min each, at room temperature -RT), isopropyl alcohol (2×30 min each, at RT), chloroform (overnight, at RT), liquid HistoPlast wax (Biopack – 2×20 min each, at 56 °C). Bladders embedded in HistoPlast were sectioned at 3 μm using a Finesse E + Microtome (Thermo Scientific) and collected in charged slides. Hematoxylin-eosin staining of sections was performed after dewaxing with xylene (3×10 min each, RT) and hydration by serial passages through 100% ethanol (2×20 min each, at RT), 96% ethanol (20 min, at RT) and water (2×5 min each, at RT). Sections were incubated with Mayer's hematoxylin for 10 min at RT, washed with tap and distilled water and then incubated with eosin for 5 min. Finally, the sections were dehydrated, mounted and visualized using an Olympus BX51 bright field microscope equipped with 4x and 10x objectives. Images were captured using an Olympus DP72 camera.

Thioflavin T stain and immunofluorescence confocal analysis

For cell lines, cells were plated on 12 mm diameter coverslips in 24-well plates at 1×10^5 cells/mL. Twenty-four hours later, cells were fixed with 4% paraformaldehyde in PBS 1X, pH 7.4 for 15 min at RT. Permeabilization was performed by incubation in 0.1% Triton X-100 in PBS for 15 min at RT. RNase A (E1008, ZymoResearch, 10 mg/mL in H_2O mQ) treatment was performed for 1 h at 37 °C. Epitope unmasking was performed at this time, if necessary, by immersing the coverslips in 70% formic acid for 40 s. For immunocytochemistry, cells were incubated in 1% BSA – 0.1% Triton X-100 in PBS (blocking buffer, BB) for 40 min at RT. Cells were exposed to specific antibodies diluted in BB overnight (ON) at 4 °C. Specific antibodies included rabbit polyclonal anti-amyloid oligomers (ab126892, Abcam), rabbit monoclonal anti-PGK1 (ab199438, Abcam), rabbit polyclonal anti-histone deacetylase 1 (HDAC1, #2062, Cell Signaling), mouse monoclonal anti-RhoA (#26904, NewEast Biosciences). Anti-antibodies (Alexa Fluor 555 goat anti-mouse -A21424- or goat anti-rabbit -A21429, Thermo Fisher Scientific) diluted at 2 μg/mL in BB were incubated for 1 h, RT. Alexa Fluor 568 phalloidin (A22283, Thermo Fisher Scientific), Alexa Fluor 633 phalloidin (A22284, Thermo Fisher Scientific) or TO-PRO-3 iodide (T3605, Thermo Fisher Scientific) counterstains were included in some experiments. Thioflavin T (ThT, 5 mM in PBS, ab120751, Abcam) incubation was performed for 15 min at RT. Coverslips were mounted in ProLong Glass Antifade Mountant (P36984, ThermoFisher Scientific).

For bladder sections, slides were deparaffinized as described above. A 5-minute incubation in 10 mM borax (71997, Sigma-Aldrich), 1 mM EDTA (Sigma-Aldrich) pH 9, was performed to reduce tissue autofluorescence. RNase treatment was also performed as previously described. ThT staining was performed using 0.5% ThT in 0.1 N HCl for 15 min at RT. For confocal imaging, slides were mounted in ProLong Glass Antifade Mountant.

Images were captured in a confocal LSM ZEISS 800 using an inverted Axio Observer 2 stand, four laser units (405, 488, 561 and 640 nm), and 10x (NA 0.3), 20x (NA 0.5), 63x (NA 1.4) and 100x (NA 1.4) objectives. Identical laser and PMT settings were used to acquire the images for comparison. Images were processed using ZEN Blue 2.3 and ImageJ software[100].

Preparation of protein homogenates

For cell lines, 1.5×10^8 cells were lysed in 500 μL of 0.25% Igepal CA-630 (Sigma-Aldrich) in Tris-buffered saline (TBS). For blood cell lysis, the total cell fraction was obtained by centrifugation at 2000 xg for 10 min at RT. The cell pellet was lysed in 0.25% Igepal CA-630-TBS. For mice bladder, 40 mg of tissue were mechanically homogenized in 400 μL of 0.25% Igepal CA-630-TBS. Homogenates were clarified by centrifugation at 9000 xg for 15 min at 4 °C and the supernatant was collected. Protein quantification was performed using Bradford reagent (114391, Sigma-Aldrich). RNA was digested by treatment with RNase A (0.1 mg/mL final concentration) at 37 °C for 20 min. Homogenates were used immediately or stored at -20 °C for a maximum of two weeks before use.

Spectrofluorimetry

Serial dilutions of protein homogenates from cell culture, blood or mice bladder were prepared in TBS starting at 3.2 mg/mL protein. ThT was freshly prepared on the day of the experiment by dissolving it in water at 100 mM and then filtering it through a 0.2 μm syringe filter. Serial dilutions of ThT starting at 400 μM were prepared in TBS. 50 μL of ThT at each concentration was mixed with 50 μL of protein dilutions and transferred to a black Nunc™ 96-well plate (Nunclon #137103, Thermo Fisher Scientific). ThT fluorescence was measured at RT in a microplate spectrophotometer (Varioskan Flash Microplate Spectrophotometer, ThermoFisher, Vantaa, Finland) using excitation at 450 nm and an emission filter at 490 ± 5 nm.

Native electrophoresis

Native electrophoresis was performed on 1.5% agarose gels. Fifteen microliters per lane of each sample (cell culture and blood homogenates RNase treated) were run for 45 min at 60 V in native buffer (25 mM Tris-HCl, 192 mM glycine, pH 8.3) until the dye front reached the edge of the gel. Homogenates digested with Proteinase K (100 μg/mL, supplemented with 1 mM $CaCl_2$) for 20 min at 37 °C was also included. The gel was incubated in fixative solution (40% ethanol, 10% acetic acid) overnight, washed 3×15 min with acidic water (0.28 mM HCl) and stained with 0.1% ThT in acidic water. Excess ThT was removed by washing 3×15 min with acidic water. Fluorescence was recorded on a FujiFilm FLA-2000 Fluorescence Image Analyzer using the FITC channel. The gel was then stained with Coomassie R-250 0.01% in fixative, destained in fixative solution and scanned using a desktop scanner.

Gel filtration analysis

Protein homogenates from HT1197 cell line were analyzed by gel filtration chromatography using a Prominence UFLC system (Shimadzu, Tokyo, Japan) with in-line photodiode array (PDA) and fluorescence (FD) detectors. Sample (150 μL) was injected into a Superdex 200 Increase 10/300 GL column (Cytiva, 28-9909-44; 10–600 kDa molecular mass range) equilibrated in 0.05 M phosphate buffer, 0.15 M NaCl, pH 7.0 at a flow rate of 0.5 mL/min. Amyloids were detected by in-line PDA (absorbance at 280 nm) and FD (excitation at 350 nm and emission at 472 nm). A calibration curve was constructed by measuring elution times of the standard (1511901, Bio Rad): thyroglobulin (670 kDa), γ-globulin (158 kDa), ovalbumin (44 kDa), myoglobin (17 kDa), and vitamin B12 (1.35 kDa).

Amyloid purification

For amyloid purification, protein homogenates (RNase treated) were seeded on 30% sucrose cushion and centrifuged in an Optima XL-100 Beckman Coulter centrifuge using an SW60 rotor for 1 h at 4 °C at 50,000 rpm. The supernatant was discarded and the pellet was resuspended in H_2O mQ. The resuspended pellet was used immediately for further analysis.

Confocal, polarized and transmission electron microscopy of purified amyloids

The purified amyloids were stained with 0.5% ThT (ab120751, Abcam) in 0.1 N HCl for 15 min at RT and observed with a LSM ZEISS 800 confocal microscope. Identical laser and PMT settings were used to acquire the images for comparison. As an alternative approach, purified amyloids were stained with 500 μM Congo Red in 80% ethanol for one hour at room temperature. Following this, the samples were centrifuged at 17,000 xg for 30 min and then resuspended and mounted in 50% glycerol. Images of Congo red birefringence were acquired using a polarized microscope. Ultracentrifugation pellet of blood from healthy donors was used as a negative control.

Electron microscopy negative staining of purified amyloids was performed at the Transmission Electron Microscopy Unit (Faculty of Science, UdelaR). Purified amyloid was centrifuged 5000 xg, 5 min at RT and the supernatant was collected. A drop of supernatant (10 μL) was applied to a Formvar/Carbon Supported Copper Grids 200 mesh (930245, Sigma-Aldrich). Samples were allowed to settle for 20 min at RT. Staining was performed immediately with 10 μL 2% uranyl acetate for 1 min and then air dried prior to observation. Samples were observed using a Joel JEM-1010 microscope.

Circular dichroism spectroscopy

Prior to Circular Dichroism (CD) spectroscopy, the amyloid pellet was resuspended in water. CD spectra were recorded using a Chirascan V100 spectrometer (Applied Photophysics) at 25 °C, with a wavelength range of 185 to 260 nm. The data presented in each spectrum represents the mean of three scans, with the corresponding buffer spectrum subtracted to correct for any background interference. The resulting data were processed and the molar ellipticity ($\Delta\varepsilon$ $M^{-1}cm^{-1}$) was plotted as a function of wavelength, assuming a scale factor of 1. Structural parameters, including β-sheet content, were determined through data analysis performed with the BeStSel web server for secondary structure estimation (https://bestsel.elte.hu/).

Dynamic light scattering (DLS)

In order to conduct DLS experiments, samples of amyloid from the EJ138, HT1197 and RT4 cell lines were subjected to centrifugation at 13,000 rpm for a period of fifteen minutes. The soluble fraction was then measured in triplicate at 25 °C in a Zetasizer Nano S (Malvern Panalytical) utilising disposable plastic cuvettes. The data was subsequently analysed with Zetasizer software v. 8.02 (Malvern Panalytical).

Differential scanning fluorimetry

The amyloid samples from the EJ138, HT1197 and RT4 cell lines were subjected to the same pre-treatment protocol as that employed for the DLS experiments. The soluble fractions were subjected to consecutive heating and cooling scans in a Prometheus NT.48 nanoDSF device (NanoTemper Technologies) at a constant rate of 1 °C per minute, spanning a temperature range from 20 °C to 95 °C. Fluorescence signals at 330 nm and 350 nm were monitored to assess protein unfolding behavior.

Dot blot assay

One microlitre of amyloid, purified by ultracentrifugation as previously described, was pipetted into nitrocellulose membranes. The membranes were blocked with blocking buffer (1% BSA in TBS-T) for a period of two hours at RT. The specific rabbit polyclonal anti-histone deacetylase 1 (HDAC1, #2062, Cell Signaling) and mouse monoclonal anti-RhoA (#26904, NewEast Biosciences) were incubated in blocking buffer for two hours at RT. Horseradish peroxidase (HRP)-conjugated anti-rabbit (#AP187P, Millipore Sigma) and (HRP)-conjugated anti-mouse (#12–349, Merck Sigma) antibodies were used, diluted in blocking buffer and incubated for one hour at RT. Signal development was performed using the Pierce™ ECL Western Blotting Substrate (ThermoFisher Scientific). The membranes were scanned in an iBright™ CL1500 Imaging System (ThermoFisher Scientific).

Mass spectrometry (MS) analysis

Protein homogenates (RNase treated) obtained from RT4 and HT1197 cells were digested with proteinase K (100 μg/mL, supplemented with 1 mM $CaCl_2$) for 20 min at 37 °C, followed sedimentation of the resistant protein structures by the above-mentioned ultracentrifugation protocol. The pellets were resuspended in either H_2O mQ (water, hereafter) or 100% formic acid, incubated for 1 h at 37 °C, and lyophilized. Dried samples were resuspended in sample buffer suitable for tricine SDS-PAGE[101]. Three independent biological replicates

were prepared. Samples were loaded onto 12% gels, allowing proteins to migrate 1 cm into the resolving gel. After Coomassie staining, gel slices were excised and sent to the proteomics facility CEQUIBIEM (QB-FCEN-UBA/IQUIBICEN-CONICET, Buenos Aires, Argentina) for further processing and mass spectrometry (MS) analysis. Gel slices were destained with ammonium bicarbonate and acetonitrile (ACN), reduced with 20 mM dithiothreitol (DTT) for 45 min at 56 °C, alkylated with 50 mM iodoacetamide for 45 min in the dark, and trypsinized overnight at 37 °C. Peptides were then extracted by sonication in 50% ACN and 0.5% trifluoroacetic acid solution, further concentrated by speed-vacuum drying, resuspended in 0.1% formic acid and desalted on Zip-Tip C18.

Liquid chromatography coupled to tandem mass spectrometry (LC-MS/MS) in a Q-Exactive instrument (ThermoFisher Scientific) was used for peptide separation and analysis. The chromatographic separation was performed in a nano-HPLC EASY-nLC 1000 (ThermoFisher Scientific), with a C18 reverse-phase column (EASY-Spray Accucore, P/N ES902) operated with a flow rate of 200 nL/min at 35 °C. The mobile phase was a two-solution system of 0.1% formic acid in water (solution A) and 0.1% formic acid in ACN (solution B). Peptides (4 μL) were injected in 100% solution A and eluted for 120 min with increasing concentrations of solution B: first 5 min in 5% B, then a 100 min gradient of 35-95% B, followed by a 5 min gradient until 95% B, and finally 10 min of isocratic elution with 95% B.

The eluting peptides entering the Q-Exactive instrument were first ionized in an EASY-SPRAY electrospray (ThermoFisher Scientific) at 2.50 kV. Only positive ions were selected in the Orbitrap analyzer, which was operated in the Full-MS and MS/MS modes. The scanned mass range was 400–2000 m/z, with a Full-MS resolution of 70,000 and a MS/MS resolution of 17,500, both at 400 m/z. The 12 most intense precursor ions in each cycle were sequentially isolated (data dependent mode), fragmented by higher energy collisional dissociation (HCD), and measured in the Orbitrap analyzer. Peptides with a charge of + 1 or with an unassigned charge state were excluded from fragmentation for MS/MS.

Analysis of MS data

Raw MS data were processed using the MaxQuant software (v. 1.6.12.0)[102]. Proteins and peptides were identified using a target-decoy approach with a false discovery rate (FDR) of 1% using the human proteome database with all known substitutions from RT4 and HT1197 cell lines[103]. The analysis was performed with almost all the default settings as follows: trypsin/P specificity for digestion with up to two missed cleavages; carbamidomethylation of cysteines as a fixed modification; N-acetylation of proteins and oxidation of methionine as variable modifications; and inclusion of the contaminant database. 'Match between runs' was enabled with a match time window of 0.7 min and an alignment time window of 15 min. Relative label-free quantification (LFQ) was performed using the MaxLFQ algorithm with a minimum ratio count of one.

MaxQuant-processed data were further analyzed using the Perseus software (v. 1.6.15.0)[104]. Student's t-test was performed for log2 transformed LFQ intensities to identify proteins with significant changes in abundance between the conditions compared. Those proteins with a fold-change > 2 were defined as differentially present between formic acid and water samples. The mass spectrometry proteomics data have been deposited to the ProteomeXchange Consortium via the PRIDE[105] partner repository with the dataset identifier PXD053864 (http://www.ebi.ac.uk/pride/archive/projects/PXD053864).

The Database for Annotation, Visualization and Integrated Discovery (DAVID) was used for enrichment analysis[106,107]. Amylpred2 tool[108] was running for aggregation-prone regions prediction, using the Aggrescan[109] and Hexapeptide Conformational Energy[43] methods. To filter out hits corresponding to signal peptides, these were predicted using SignalP 6.0[110]. A KEGG Mapper search[111] was used to associate identified proteins to molecular networks[112–114]. Analysis of dataset overlap between RT4 and HT1197 amyloid-identified proteins and tumor suppressors (https://bioinfo.uth.edu/TSGene/), oncogenes (https://ongene.bioinfo-minzhao.org/tutorial.html) and bladder cancer drivers (https://www.intogen.org/search?cancer=BLCA) was performed using the Interactive web tool[115].

Statistical analysis

All experiments were performed with a minimum of three biological replicates. D'Agostino & Pearson and Shapiro-Wilk tests were used to assess data normality and behavior. One-way analysis of variance (ANOVA) and Tukey's multiple comparison test were also used to analyze the data.

Data availability

References

1. Riek, R. The three-dimensional structures of amyloids. *Cold Spring Harb Perspect. Biol.* **9** (2017).
2. Goldschmidt, L., Teng, P. K., Riek, R. & Eisenberg, D. Identifying the amylome, proteins capable of forming amyloid-like fibrils. *Proc. Natl. Acad. Sci. U. S. A.* **107**, 3487–3492 (2010).
3. Taylor, A. I. P. & Staniforth, R. A. General principles underpinning amyloid structure. *Front. Neurosci.* **16** (2022).
4. Otzen, D. & Riek, R. Functional amyloids. *Cold Spring Harb. Perspect. Biol.* **11** (2019).
5. Akbey, Ü. & Andreasen, M. Functional amyloids from bacterial biofilms – structural properties and interaction partners. *Chem. Sci.* **13**, 6457 (2022).
6. Maji, S. K. et al. Functional amyloids as natural storage of peptide hormones in pituitary secretory granules. *Science* **325**, 328–332 (2009).

7. Sudhakaran, I. P. & Ramaswami, M. Long-term memory consolidation: the role of RNA-binding proteins with prion-like domains. *RNA Biol.* **14**, 568–586 (2017).
8. Dobson, C. M. The amyloid phenomenon and its links with human disease. *Cold Spring Harb. Perspect. Biol.* **9** (2017).
9. Navalkar, A. et al. Direct evidence of cellular transformation by prion-like p53 amyloid infection. *J. Cell. Sci.* **134** (2021).
10. Li, J. et al. p53 amyloid aggregation in cancer: function, mechanism, and therapy. *Exp. Hematol. Oncol.* **11** (2022).
11. Levy, C. B. et al. Co-localization of mutant p53 and amyloid-like protein aggregates in breast tumors. *Int. J. Biochem. Cell. Biol.* **43**, 60–64 (2011).
12. Lasagna-Reeves, C. A. et al. Dual role of p53 amyloid formation in cancer; loss of function and gain of toxicity. *Biochem. Biophys. Res. Commun.* **430**, 963–968 (2013).
13. Sengupta, S. et al. p53 amyloid pathology is correlated with higher cancer grade irrespective of the mutant or wild-type form. *J. Cell. Sci.* **136** (2023).
14. De Smet, F. et al. Nuclear inclusion bodies of mutant and wild-type p53 in cancer: a hallmark of p53 inactivation and proteostasis remodelling by p53 aggregation. *J. Pathol.* **242**, 24–38 (2017).
15. Sengupta, S., Ghufran, S. M., Khan, A., Biswas, S. & Roychoudhury, S. Transition of amyloid/mutant p53 from tumor suppressor to an oncogene and therapeutic approaches to ameliorate metastasis and cancer stemness. *Cancer Cell Int.* **22**, 1–18 (2022).
16. Saginala, K. et al. Epidemiology of bladder cancer. *Med. Sci.* **8** (2020).
17. Grabe-Heyne, K. et al. Intermediate and high-risk non-muscle-invasive bladder cancer: an overview of epidemiology, burden, and unmet needs. *Front. Oncol.* **13** (2023).
18. Ripoll, J. et al. Cancer-specific survival by stage of bladder cancer and factors collected by Mallorca Cancer Registry associated to survival. *BMC Cancer* **21** (2021).
19. Patel, V. G., Oh, W. K. & Galsky, M. D. Treatment of muscle-invasive and advanced bladder cancer in 2020. *CA Cancer J. Clin.* **70**, 404–423 (2020).
20. Jubber, I. et al. Epidemiology of bladder Cancer in 2023: a systematic review of risk factors. *Eur. Urol.* **84**, 176–190 (2023).
21. Hayashi, T. et al. Mutational landscape and environmental effects in bladder cancer. *Int. J. Mol. Sci.* **21**, 1–14 (2020).
22. Powles, T. et al. Bladder cancer: ESMO Clinical Practice Guideline for diagnosis, treatment and follow-up ☆. *Ann. Oncol.* **33**, 244–258 (2022).
23. Schwarzova, L., Novakova, V., Danisovic, Z., Ziaran, S. & L. & Molecular classification of urothelial bladder carcinoma. *Mol. Biol. Rep.* **50**, 7867–7877 (2023).
24. Goto, T. & Miyamoto, H. Why has the prognosis for muscle-invasive bladder cancer not significantly improved after decades of therapeutic advancements? *Expert Rev. Anticancer Ther.* **20**, 229–231 (2020).
25. Rigby, C. C. & Franks, L. M. A human tissue culture cell line from a transitional cell tumour of the urinary bladder: growth, chromosone pattern and ultrastructure. *Br. J. Cancer* **24**, 746–754 (1970).
26. Bubeník, J. et al. Established cell line of urinary bladder carcinoma (T24) containing tumour-specific antigen. *Int. J. Cancer* **11**, 765–773 (1973).
27. Rasheed, S., Gardner, M. B., Rongey, R. W., Nelson-Rees, W. A. & Arnstein, P. Human bladder carcinoma: characterization of two new tumor cell lines and search for tumor viruses. *J. Natl. Cancer Inst.* **58**, 881–890 (1977).
28. Biancalana, M. & Koide, S. Molecular mechanism of Thioflavin-T binding to amyloid fibrils. *Biochim. et Biophys. Acta Proteins Proteom.* **1804**, 1405–1412 (2010).
29. Naiki, H., Higuchi, K., Hosokawa, M. & Takeda, T. Fluorometric determination of amyloid fibrils in vitro using the fluorescent dye, thioflavine T. *Anal. Biochem.* **177**, 244–249 (1989).
30. Xue, C., Lin, T. Y., Chang, D. & Guo, Z. Thioflavin T as an amyloid dye: Fibril quantification, optimal concentration and effect on aggregation. *R. Soc. Open Sci.* **4** (2017).
31. Gui, X. et al. Liquid-liquid phase separation of amyloid-β oligomers modulates amyloid fibrils formation. *J. Biol. Chem.* **299** (2023).
32. Ambadipudi, S., Biernat, J., Riedel, D., Mandelkow, E. & Zweckstetter, M. Liquid-liquid phase separation of the microtubule-binding repeats of the Alzheimer-related protein tau. *Nat. Commun.* **8** (2017).
33. Ray, S. et al. α-Synuclein aggregation nucleates through liquid–liquid phase separation. *Nat. Chem.* **12**, 705–716 (2020).
34. Lan, J. et al. The peripheral blood of Aβ binding RBC as a biomarker for diagnosis of Alzheimer's disease. *Age Ageing.* **44**, 458–464 (2015).
35. Fitzpatrick, A. W. & Saibil, H. R. Cryo-EM of amyloid fibrils and cellular aggregates. *Curr. Opin. Struct. Biol.* **58**, 34–42 (2019).
36. Ruiz-Ortega, E. D., Wilkaniec, A. & Adamczyk, A. Liquid–liquid phase separation and conformational strains of α-Synuclein: implications for Parkinson's disease pathogenesis. *Front. Mol. Neurosci.* **17**, 1494218 (2024).
37. Randrianjatovo-Gbalou, I., Marcato-Romain, C. E. & Girbal-Neuhauser, E. Quantification of amyloid fibrils using size exclusion chromatography coupled with online fluorescence and ultraviolet detection. *Anal. Biochem.* **488**, 19–21 (2015).
38. Upadhyay, A., Vassar, R. J & Savas, J. N. Biochemical purification and proteomic characterization of amyloid fibril cores from the brain. *J. Vis. Exp.* **2022** (2022).
39. Crespo, R. et al. What can the kinetics of amyloid fibril formation tell about off-pathway aggregation? *J. Biol. Chem.* **291**, 2018–2032 (2016).
40. Balobanov, V. et al. The kinetics of amyloid fibril formation by de novo protein albebetin and its mutant variants. *Biomolecules* **10**, 241 (2020).
41. Ghosh, D. et al. Structure based aggregation studies reveal the presence of helix-rich intermediate during α-Synuclein aggregation. *Sci. Rep* **51** (5), 1–15 (2015).
42. Farris, F. et al. Unveiling the mechanistic link between extracellular amyloid fibrils, mechano-signaling and YAP activation in cancer. *Cell. Death Dis.* **151**, 1–13 (2024).
43. Zhang, Z., Chen, H. & Lai, L. Identification of amyloid fibril-forming segments based on structure and residue-based statistical potential. *Bioinformatics* **23**, 2218–2225 (2007).
44. Li, Y. et al. Conformable self-assembling amyloid protein coatings with genetically programmable functionality. *Sci. Adv.* **6** (2020).
45. Upadhyay, A. et al. Amyloid fibril proteomics of AD brains reveals modifiers of aggregation and toxicity. *Mol. Neurodegener.* **18** (2023).
46. Hamburg, D. M., Suh, M. J. & Limbach, P. A. Limited proteolysis analysis of the ribosome is affected by subunit association. *Biopolymers* **91**, 410–422 (2009).
47. Suh, M. J., Pourshahian, S. & Limbach, P. A. Developing limited proteolysis and mass spectrometry for the characterization of ribosome topography. *J. Am. Soc. Mass. Spectrom.* **18**, 1304–1317 (2007).
48. Hazeki, N., Tukamoto, T., Goto, J. & Kanazawa, I. Formic acid dissolves aggregates of an N-terminal huntingtin fragment containing an expanded polyglutamine tract: applying to quantification of protein components of the aggregates. *Biochem. Biophys. Res. Commun.* **277**, 386–393 (2000).
49. Christensen, L. F. B., Nowak, J. S., Sønderby, T. V., Frank, S. A. & Otzen, D. E. Quantitating denaturation by formic acid: imperfect repeats are essential to the stability of the functional amyloid protein FapC. *J. Biol. Chem.* **295**, 13036–13041 (2020).
50. Casali, B. T. & Landreth, G. E. Aβ extraction from murine brain homogenates. *Bio-protocol* 6 (2016).
51. Christensen, D. Z., Bayer, T. A. & Wirths, O. Formic acid is essential for immunohistochemical detection of aggregated intraneuronal Aβ peptides in mouse models of Alzheimer's disease. *Brain Res.* **1301**, 116–125 (2009).

52. Balani, S., Nguyen, L. V. & Eaves, C. J. Modeling the process of human tumorigenesis. *Nat. Commun.* **8** (2017).
53. Chaffer, C. L. & Weinberg, R. A. How does multistep tumorigenesis really proceed? *Cancer Discov.* **5**, 22–24 (2015).
54. Ostroverkhova, D., Przytycka, T. M. & Panchenko, A. R. Cancer driver mutations: predictions and reality. *Trends Mol. Med.* **29**, 554–566 (2023).
55. Negrini, S., Gorgoulis, V. G. & Halazonetis, T. D. Genomic instability — an evolving hallmark of cancer. *Nat. Rev. Mol. Cell Biol.* **11**, 220–228 (2010).
56. Bi, Q. et al. Tumor-associated inflammation: The tumor-promoting immunity in the early stages of tumorigenesis. *J. Immunol. Res.* **2022** (2022).
57. Almagro, J., Messal, H. A., Elosegui-Artola, A., van Rheenen, J. & Behrens, A. Tissue architecture in tumor initiation and progression. *Trends Cancer* **8**, 494–505 (2022).
58. Hui, L. & Chen, Y. Tumor microenvironment: sanctuary of the devil. *Cancer Lett.* **368**, 7–13 (2015).
59. Pienta, K. J. et al. Convergent evolution, evolving evolvability, and the origins of lethal cancer. *Mol. Cancer Res.* **18**, 801–810 (2020).
60. Shomar, A. & Barak, O. & Brenner, N. Cancer progression as a learning process. *iScience* **25** (2022).
61. Ano Bom, A. P. D. et al. Mutant p53 aggregates into prion-like amyloid oligomers and fibrils: implications for cancer. *J. Biol. Chem.* **287**, 28152–28162 (2012).
62. Degoricija, M. et al. The dynamics of the inflammatory response during BBN-induced bladder carcinogenesis in mice. *J. Transl. Med.* **17** (2019).
63. Fantini, D. et al. A carcinogen-induced mouse model recapitulates the molecular alterations of human muscle invasive bladder cancer. *Oncogene* **37**, 1911–1925 (2018).
64. Gottwald, J. & Röcken, C. The amyloid proteome: a systematic review and proposal of a protein classification system. *Crit. Rev. Biochem. Mol. Biol.* **56**, 526–542 (2021).
65. Drummond, E. et al. The amyloid plaque proteome in early onset Alzheimer's disease and down syndrome. *Acta Neuropathol. Commun.* **10** (2022).
66. Liao, L. et al. Proteomic characterization of postmortem amyloid plaques isolated by laser capture microdissection. *J. Biol. Chem.* **279**, 37061–37068 (2004).
67. Xiong, F., Ge, W. & Ma, C. Quantitative proteomics reveals distinct composition of amyloid plaques in Alzheimer's disease. *Alzheimers Dement.* **15**, 429–440 (2019).
68. Xia, Q. et al. Proteomic identification of novel proteins associated with Lewy bodies. *Front. Biosci.* **13**, 3850–3856 (2008).
69. Ulamec, S. M., Brockwell, D. J. & Radford, S. E. Looking beyond the core: the role of flanking regions in the aggregation of amyloidogenic peptides and proteins. *Front. Neurosci.* **14** (2020).
70. Olzscha, H. et al. Amyloid-like aggregates sequester numerous metastable proteins with essential cellular functions. *Cell* **144**, 67–78 (2011).
71. Low, K. J. Y., Venkatraman, A., Mehta, J. S. & Pervushin, K. Molecular mechanisms of amyloid disaggregation. *J. Adv. Res.* **36**, 113 (2022).
72. Eisenberg, D. S. & Sawaya, M. R. Structural studies of amyloid proteins at the molecular level. *Annu. Rev. Biochem.* **86**, 69–95 (2017).
73. Qiu, A. et al. Phosphoglycerate kinase 1: an effective therapeutic target in cancer. *Front. Biosci. Landmark.* **29**, 92 (2024).
74. Valentini, G., Maggi, M. & Pey, A. L. Protein Stability, folding and misfolding in human PGK1 deficiency. *Biomolecules* **3**, 1030–1052 (2013).
75. Pey, A. L., Maggi, M. & Valentini, G. Insights into human phosphoglycerate kinase 1 deficiency as a conformational disease from biochemical, biophysical, and in vitro expression analyses. *J. Inherit. Metab. Dis.* **37**, 909–916 (2014).
76. Rahman, M. M. & Lendel, C. Extracellular protein components of amyloid plaques and their roles in Alzheimer's disease pathology. *Mol. Neurodegener.* **16** (2021).
77. Kim, J. M. et al. Identification of genes related to Parkinson's disease using expressed sequence tags. *DNA Res.* **13**, 275–286 (2006).
78. Sakaue, S. et al. Early-onset parkinsonism in a pedigree with phosphoglycerate kinase deficiency and a heterozygous carrier: do PGK-1 mutations contribute to vulnerability to parkinsonism? *NPJ Park Dis.* **31** (3), 1–3 (2017).
79. Virmani, T. et al. Levodopa responsive parkinsonism in two patients with phosphoglycerate kinase deficiency. *Mov. Disord. Clin. Pract.* **1**, 240–242 (2014).
80. Sotiriou, E., Greene, P., Krishna, S., Hirano, M. & DiMauro, S. Myopathy and parkinsonism in phosphoglycerate kinase deficiency. *Muscle Nerve* **41**, 707–710 (2010).
81. Konrad, P. N., McCarthy, D. J., Mauer, A. M., Valentine, W. N. & Paglia, D. E. Erythrocyte and leukocyte phosphoglycerate kinase deficiency with neurologic disease. *J. Pediatr.* **82**, 456–460 (1973).
82. Chiarelli, L. R. et al. Molecular insights on pathogenic effects of mutations causing phosphoglycerate kinase deficiency. *PLoS One* **7**, e32065 (2012).
83. Fiorillo, A. et al. The phosphoglycerate kinase 1 variants found in carcinoma cells display different catalytic activity and conformational stability compared to the native enzyme. *PLoS One* **13**, (2018).
84. He, Y. et al. PGK1-mediated cancer progression and drug resistance. *Am. J. Cancer Res.* **9**, 2280 (2019).
85. Zhang, K., Sun, L. & Kang, Y. Regulation of phosphoglycerate kinase 1 and its critical role in cancer. *Cell. Commun. Signal.* **21**, 1–15 (2023).
86. Datta, N., Chakraborty, S., Basu, M. & Ghosh, M. K. Tumor suppressors having oncogenic functions: the double agents. *Cells* **10**, 1–26 (2020).
87. Kelly, R. D. W. & Cowley, S. M. The physiological roles of histone deacetylase (HDAC) 1 and 2: complex co-stars with multiple leading parts. *Biochem. Soc. Trans.* **41**, 741–749 (2013).
88. Brancolini, C., Gagliano, T. & Minisini, M. HDACs and the epigenetic plasticity of cancer cells: target the complexity. *Pharmacol. Ther.* **238**, 108190 (2022).
89. Pinkerneil, M. et al. Inhibition of class I histone deacetylases 1 and 2 promotes urothelial carcinoma cell death by various mechanisms. *Mol. Cancer Ther.* **15**, 299–312 (2016).
90. Jaffe, A. B. & Hall, A. Rho GTPases: biochemistry and biology. *Annu. Rev. Cell. Dev. Biol.* **21**, 247–269 (2005).
91. O'Connor, K. L. & Chen, M. Dynamic functions of RhoA in tumor cell migration and invasion. *Small GTPases.* **4**, 141 (2013).
92. Blake, D. R. & Der, C. J. RHOA mutations in cancer: oncogenes or tumor suppressors? *Rho GTPases Mol. Biol. Heal. Dis.* 121–138. https://doi.org/10.1142/9789813228795_0007 (2017).
93. Yan, G. et al. Silencing RhoA inhibits migration and invasion through Wnt/β-catenin pathway and growth through cell cycle regulation in human tongue cancer. *Acta Biochim. Biophys. Sin. (Shanghai)* **46**, 682–690 (2014).
94. Simpson, K. J., Dugan, A. S. & Mercurio, A. M. Functional analysis of the contribution of RhoA and RhoC GTPases to invasive breast carcinoma. *Cancer Res.* **64**, 8694–8701 (2004).
95. Schmidt, L. J. et al. RhoA as a mediator of clinically relevant androgen action in prostate cancer cells. *Mol. Endocrinol.* **26**, 716 (2012).
96. Faustmann, P. *The role of Grainyhead-like 3 Transcription Factor* (Ulm University, 2023).
97. Šulskis, D., Žiaunys, M., Sakalauskas, A., Sniečkute, R. & Smirnovas, V. Formation of amyloid fibrils by the regulatory 14-3-3ζ protein. *Open. Biol.* **14** (2024).
98. Takamatsu, Y., Ho, G. & Hashimoto, M. Amyloid evolvability and cancer. *Trends Cancer* **6**, 624–627 (2020).

99. Ding, H. et al. Serum amyloid a predicts prognosis and chemotherapy efficacy in patients with advanced pancreatic cancer. *J. Inflamm. Res.* **16**, 1297 (2023).
100. Schindelin, J. et al. Fiji: an open-source platform for biological-image analysis. *Nat. Methods* **9**, 676–682 (2012).
101. Schägger, H. Tricine-SDS-PAGE. *Nat. Protoc.* **1**, 16–22 (2006).
102. Tyanova, S., Temu, T. & Cox, J. The MaxQuant computational platform for mass spectrometry-based shotgun proteomics. *Nat. Protoc.* **11**, 2301–2319 (2016).
103. Tsherniak, A. et al. Defining a cancer dependency map. *Cell* **170**, 564–576e16 (2017).
104. Tyanova, S. et al. The Perseus computational platform for comprehensive analysis of (prote)omics data. *Nat. Methods.* **13**, 731–740 (2016).
105. Perez-Riverol, Y. et al. The PRIDE database resources in 2022: a hub for mass spectrometry-based proteomics evidences. *Nucleic Acids Res.* **50**, D543–D552 (2022).
106. Huang, D. W., Sherman, B. T. & Lempicki, R. A. Systematic and integrative analysis of large gene lists using DAVID bioinformatics resources. *Nat. Protoc.* **4**, 44–57 (2009).
107. Sherman, B. T. et al. DAVID: a web server for functional enrichment analysis and functional annotation of gene lists (2021 update). *Nucleic Acids Res.* **50**, W216–W221 (2022).
108. Tsolis, A. C., Papandreou, N. C., Iconomidou, V. A. & Hamodrakas, S. J. A Consensus method for the prediction of 'Aggregation-Prone' peptides in globular proteins. *PLoS One* **8**, (2013).
109. Conchillo-Solé, O. et al. AGGRESCAN: a server for the prediction and evaluation of 'hot spots' of aggregation in polypeptides. *BMC Bioinform.* **8** (2007).
110. Teufel, F. et al. SignalP 6.0 predicts all five types of signal peptides using protein language models. *Nat. Biotechnol.* **40**, 1023–1025 (2022).
111. Kanehisa, M., Sato, Y. & Kawashima, M. KEGG mapping tools for uncovering hidden features in biological data. *Protein Sci.* **31**, 47–53 (2022).
112. Kanehisa, M. & Goto, S. KEGG: kyoto encyclopedia of genes and genomes. *Nucleic Acids Res.* **28**, 27–30 (2000).
113. Kanehisa, M. Toward understanding the origin and evolution of cellular organisms. *Protein Sci.* **28**, 1947–1951 (2019).
114. Kanehisa, M., Furumichi, M., Sato, Y., Kawashima, M. & Ishiguro-Watanabe M. KEGG for taxonomy-based analysis of pathways and genomes. *Nucleic Acids Res.* **51**, D587–D592 (2023).
115. Heberle, H. et al. A web-based tool for the analysis of sets through Venn diagrams. *BMC Bioinform.* **16**, 1–7 (2015).

Acknowledgements

Author contributions

L.C. performed all the experiments and acquired the data. D.A. performed the spectrofluorometric, gel filtration, native electrophoresis and amyloid proteome experiments. C.X.G-L. performed the MS analysis. F.G. and D.C. provided bladder murine staining, data analysis and pathological interpretation. H.P-E., F.G. and M.N.C. performed the BBN-generated model. C.V. performed the gel filtration experiments. M.F. and F.C. performed CD, DSL and nanoDSF experiments. D.A., L.C., C.X.G-L., F. G., D.C., J.F., H.P-E., C.V., I.L., S.C-S., B.I., and K.M. discussed results and provided manuscript feedback. DA, LC designed the experiments, analyzed and interpreted the data, conducted scientific direction and wrote the manuscript.

Declarations

Competing interests

The authors declare no competing interests.

Additional information

Supplementary Information The online version contains supplementary material available at https://doi.org/10.1038/s41598-025-88307-7.

Correspondence and requests for materials should be addressed to D.A. or L.C.

Reprints and permissions information is available at www.nature.com/reprints.

Publisher's note Springer Nature remains neutral with regard to jurisdictional claims in published maps and institutional affiliations.